JOURNAL OF SYNCHROTRON RADIATION

ISSN 1600-5775

Received 26 October 2016
Accepted 25 April 2017

Edited by A. F. Craievich, University of São Paulo, Brazil

Keywords: XAS; *in situ*; EXAFS; XANES; core–shell.

Supporting information: this article has supporting information at journals.iucr.org/s

Insight into growth of Au–Pt bimetallic nanoparticles: an *in situ* XAS study

Chandrani Nayak,[a,b] D. Bhattacharyya,[a]* K. Bhattacharyya,[c] A. K. Tripathi,[c] R. D. Bapat,[d] S. N. Jha[a] and N. K. Sahoo[a]

[a]Atomic and Molecular Physics Division, Bhabha Atomic Research Centre, Mumbai 400 085, India, [b]Homi Bhabha National Institute, Mumbai 400 094, India, [c]Chemistry Division, Bhabha Atomic Research Centre, Mumbai 400 085, India, and [d]Department of Condensed Matter Physics and Materials Science, Tata Institute of Fundamental Research, Mumbai 400005, India. *Correspondence e-mail: dibyendubarc@gmail.com

Au–Pt bimetallic nanoparticles have been synthesized through a one-pot synthesis route from their respective chloride precursors using block copolymer as a stabilizer. Growth of the nanoparticles has been studied by simultaneous *in situ* measurement of X-ray absorption spectroscopy (XAS) and UV–Vis spectroscopy at the energy-dispersive EXAFS beamline (BL-08) at Indus-2 SRS at RRCAT, Indore, India. *In situ* XAS spectra, comprising both X-ray near-edge structure (XANES) and extended X-ray absorption fine-structure (EXAFS) parts, have been measured simultaneously at the Au and Pt L_3-edges. While the XANES spectra of the precursors provide real-time information on the reduction process, the EXAFS spectra reveal the structure of the clusters formed in the intermediate stages of growth. This insight into the formation process throws light on how the difference in the reduction potential of the two precursors could be used to obtain the core–shell-type configuration of a bimetallic alloy in a one-pot synthesis method. The core–shell-type structure of the nanoparticles has also been confirmed by *ex situ* energy-dispersive spectroscopy line-scan and X-ray photoelectron spectroscopy measurements with *in situ* ion etching on fully formed nanoparticles.

1. Introduction

In recent years, bimetallic nanoparticles (NPs) have attracted considerable attention in the scientific community due to their unique properties and multiple functionalities in the field of catalysis, electrochemistry and environmental science (Stamenkovic *et al.*, 2007; Tao *et al.*, 2008; Lim *et al.*, 2009; Omori *et al.*, 2011; González *et al.*, 2011). In catalysis, bimetallic NPs show improved activity and selectivity compared with their monometallic constituents (Toshima & Yonezawa, 1998; Toshima *et al.*, 1989; Zhang *et al.*, 2011*a*,*b*, 2012). For example, Au–Pt bimetallic NPs show higher CO oxidation activity relative to Au and Pt monometallic NPs (Lang *et al.*, 2004). Ataee-Esfahani *et al.* (2010*a*) have shown that Au–Pt NPs with dendritic Pt shells and Au cores show high activity as an electrocatalyst for methanol oxidation reaction also. Zhang & Toshima (2013) have demonstrated higher activity of Au/Pt bimetallic alloys for aerobic glucose oxidation. These studies inculcate the idea that alloying Au with Pt improves the activity and selectivity of the catalyst. However, the performance of the catalyst also depends on the shape, size and configuration of the bimetallic NPs. The bimetallic NPs can exist in a wide range of sizes (1–100 nm), can adopt different shapes (spherical, polyhedral, nanorod, dendritic and tripod) and can exist in different configurations (random, intermetallic, core–shell, *etc.*) (Frenkel, 2012; Liu *et al.*, 2012;

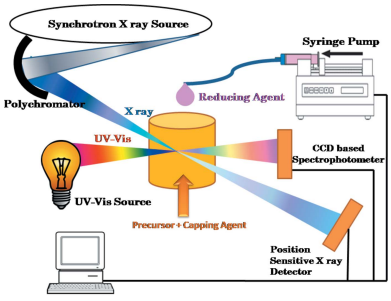

Sankar *et al.*, 2012). The existence of these particles in a wide spectrum of sizes, shapes and configurations opens up the scope of material engineering to tailor material properties based on various applications. Since the sizes, shapes and configurations in which the bimetallic NPs exist solely depends on the synthesis route which in turn affects the properties of the NPs, a rigorous *in situ* study of the synthesis process is extremely important in order to synthesize tailor-made bimetallic NPs.

Recently, with the advent of synchrotron sources, time-resolved X-ray absorption spectroscopy (XAS), which consists of two techniques, *viz.* X-ray near-edge structure (XANES) and extended X-ray absorption fine-structure (EXAFS), has become a popular tool for studying the reaction processes *in situ* which can give an insight into the structural aspects of the nucleation and growth process of NPs (Polte *et al.*, 2010; Ohyama *et al.*, 2011; Ma *et al.*, 2013; Lin *et al.*, 2006; Harada & Kamigaito, 2012; Boita *et al.*, 2014). XAS is an excellent technique for studying the bimetallic nanoparticle system due to its local structure sensitivity, element specificity and high spatial resolution. The local structure information of different elements of the bimetallic NPs can be obtained through XAS analysis which can throw light on the structure and configuration of these nanoparticle systems. *In situ* XAS can provide information on how these bimetallic NPs are formed which in turn will be helpful in designing and synthesizing NPs of desired properties. For example, Chen *et al.* (2007) have performed *in situ* EXAFS on Pd–Au NPs which revealed the formation of Pd–Au bimetallic clusters with various Pd–Au atomic stackings by properly performing hydrazine reduction and redox trans-metallation reactions.

In our earlier communication (Nayak *et al.*, 2016), we investigated the growth of block copolymer stabilized gold and platinum monometallic NPs. We were able to identify the different stages of growth and stabilization, including the various clusters formed during the growth of NPs. In the present study, we are taking one step ahead to throw light on the growth of Au–Pt bimetallic NPs stabilized by block copolymer. In most cases bimetallic NPs are synthesized by a two-step process where the seeds are first formed and then coated with the shell. However, recently, Ataee-Esfahani *et al.* (2010*a*,*b*) have developed a one-pot synthesis technique for Au–Pt bimetallic alloys using block copolymers as surfactants. This surfactant-assisted synthesis is not only convenient and environmentally friendly but can also give rise to nano-structures in the shell. Therefore, *in situ* study of this synthesis route can provide further insight which can help to make this more application-oriented.

In the present study, Au–Pt bimetallic NPs are synthesized following the one-pot synthesis route using ascorbic acid as the reducing agent and P85 block copolymer as the stabilizing agent. The synthesis process has been investigated by *in situ* XAS (XANES and EXAFS) and UV–Vis measurements simultaneously. *Ex situ* high-resolution transmission electron microscopy (HRTEM) along with energy-dispersive spectroscopy line-scan and X-ray photoelectron spectroscopy (XPS) measurements with *in situ* etching have also been carried out on the samples to complement the results.

2. Experimental

2.1. Sample preparation

Gold platinum core–shell NPs have been synthesized by mixing 2 ml of 60 m*M* chloroauric acid ($HAuCl_4.3H_2O$), 2 ml of 60 m*M* chloroplatinic acid ($H_2PtCl_6.6H_2O$) with 1 ml of 1 *M* ascorbic acid (AA) and 1 ml of 10 m*M* P85 block copolymer. The solution was stirred continuously at room temperature. As soon as the reducing agent AA was added to the solution, the colour of the solution immediately turned dark violet manifesting growth of Au NPs. After ∼20 s the colour of the solution started changing to brown and after ∼50 s the colour became black as shown in Fig. 1, manifesting formation of the Pt shells on Au cores.

For the present study, the above synthesis process has been carried out in a specially designed Teflon reaction cell having paths for both X-rays and UV–Vis radiation in mutually perpendicular directions, as shown in the schematics in Fig. 2. X-rays are transmitted through Kapton windows while the optical light is passed using optical fibres which are capped with Teflon ferrules and are directly immersed in the solution. The cell has been designed and fabricated in such a way that the optical paths can vary from 5 mm to 20 mm for X-rays and from 2 mm to 20 mm for UV–Vis radiation. The volume of the cell is defined according to the adjustment of the Kapton windows and optical fibers. The *in situ* reaction cell has been placed on a magnetic stirrer for mixing the reaction solution. The precursors (chloroauric, chloroplatinic acid and P85 block copolymer) are taken into the Teflon reaction cell and the reducer (ascorbic acid) is injected into it through a Teflon tube

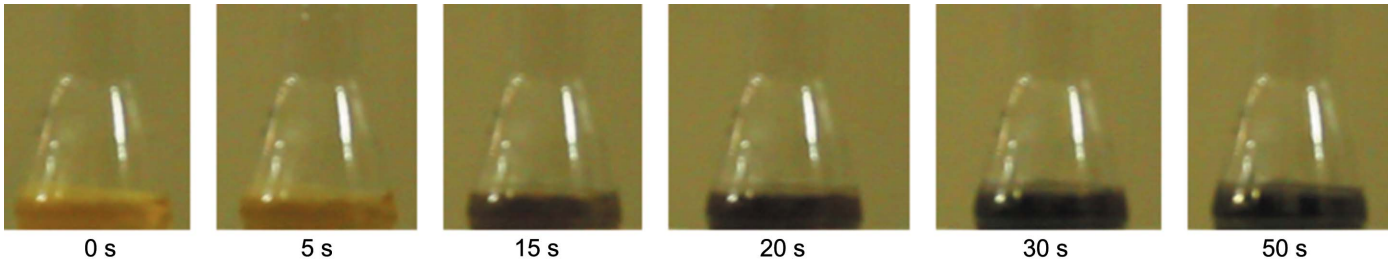

Figure 1
Photographs showing the colour of the solution at different stages during the formation of Au–Pt core–shell NPs.

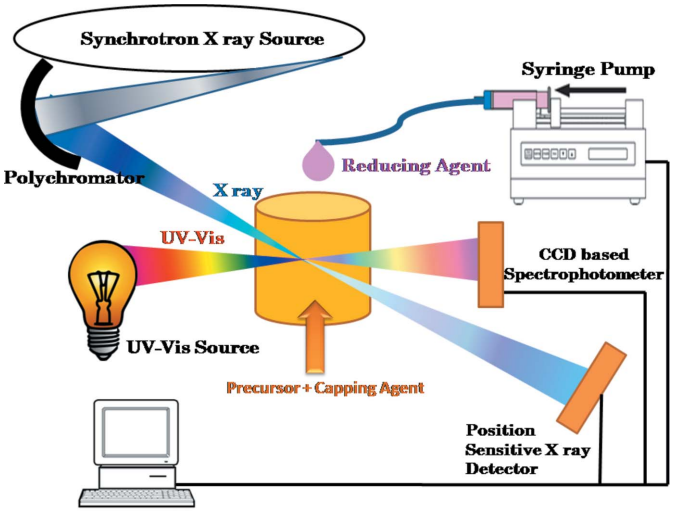

Figure 2
Schematic diagram of the experimental setup.

using a computer-controlled motor-driven syringe pump. The reducer is injected at a speed of 5 ml min^{-1} and the reaction solution is stirred at a speed of about 60 r.p.m. to have a homogeneous solution. A photograph of the experimental setup for simultaneous time-resolved EXAFS measurement and UV–Visible absorption measurement is given by Nayak *et al.* (2016).

2.2. Characterization

In the present study, the growth of NPs was characterized by taking the chloride precursors in the Teflon reaction cell described above and, as the reaction proceeds, *in situ* XAS and UV–Vis spectroscopy measurements were carried out at regular time intervals starting from the instant of adding the reducers to the respective precursors.

Time-resolved XAS measurements were carried out at the energy-dispersive EXAFS beamline (BL-8) at the Indus-2 synchrotron source (2.5 GeV, 100 mA) at the Raja Ramanna Centre for Advanced Technology (RRCAT), Indore, India (Bhattacharyya *et al.*, 2009). The above beamline works in energy-dispersive mode employing an elliptically bent 460 mm-long Si(111) polychromator and a position-sensitive detector (Das *et al.*, 2004) so that the whole absorption spectrum can be recorded simultaneously within a fraction of a second. For *in situ* XAS measurements, the Teflon reaction cell described above was placed at the sample position of the beamline and the Kapton windows of the cell were adjusted to obtain an optical path length of 10 mm for X-rays through the solution.

For XAS measurement at the Au and Pt L_3-edges the radiation transmitted through the sample is detected by a position-sensitive Mythen detector (Dectris, Switzerland). The Mythen detector is a one-dimensional X-ray detector containing 1280 silicon microstrips. It operates in single-photon-counting mode thus leading to no readout noise. For each spectrum the exposure time has been fixed to 1 s to improve the signal-to-noise ratio and XAS spectra have been recorded every second for 1 h. The beamline configuration was adjusted in such a way that XAS spectra at both the Au L_3-edge at ∼11910 eV and the Pt L_3-edge at ∼11570 eV can be measured simultaneously at the position-sensitive detector with a spreading of the energy band at a rate of ∼1 eV $pixel^{-1}$. UV–Vis absorption measurements have been carried out simultaneously with the XAS measurements using an optical-fiber-based spectrometer (Avantes, The Netherlands) where the optical fiber tips are capped with Teflon ferrules and are directly immersed in the solution. Light from the source is transmitted to the solution through the optical fiber and is collected by another optical fiber to the spectrometer. The path of the beam inside the liquid is 5 mm. UV–Vis spectra have been collected at an interval of 1 s for 30 min.

High-resolution scanning transmission electron microscope (HR-STEM) images on the above samples have been acquired with a probe-corrected 80-300 Titan TEM at 300 kV using a HAADF detector. Metal NPs, after 60 min of reaction, have been collected, washed, centrifuged and then re-dispersed in water by ultrasonicating for 20 min. A drop of this solution was placed on a copper grid, dried at room temperature and then imaged by TEM.

Energy-dispersive spectroscopy (EDS) line scan for elemental mapping was carried out on a nanocrystal in the same setup using an EDAX 30 mm Si–Li detector by tilting the sample by 20° to maximize the collection of X-rays.

Ex situ X-ray photoelectron spectroscopy (XPS) measurements were carried out on Au–Pt bimetallic NPs using a SPECS XPS setup with a PHOBIOS 100/150 delay line detector and Al $K\alpha$ (1486.6 eV) dual anode as the source. As an internal reference for the absolute binding energy, the C 1*s* peak (284.5 eV) was used. The Au–Pt bimetallic particles were etched in the preparation chamber using an IQE-IIA Specs model ion source unit having ion energy of 2 keV, operating at a filament current of 6 mA. The XPS spectra were recorded on the as-prepared sample as well as on the etched sample after different periods of etching.

3. Results and discussions

Fig. 3 shows the UV–Vis spectra of the reaction solution recorded at a time interval of 1 s during the growth of bimetallic NPs. It has been observed that at 25 s a hump appears near 540 nm which corresponds to the surface plasmon resonance (SPR) peak of gold NPs. The intensity of the Au SPR peak increases until 50 s which indicates the formation of gold NPs in the solution. However, at 100 s it can be seen that the Au SPR peak intensity decreases and it splits into a double hump. As time proceeds further the intensity of this peak decreases and finally, after 160 s, the SPR signal almost vanishes. This decrease in the intensity of the Au SPR peak and finally its disappearance indicates the formation of Pt shells on Au cores (Ataee-Esfahani *et al.*, 2010*b*; Banerjee *et al.*, 2015; Khalid *et al.*, 2010; Qian *et al.*, 2006). Thus, from the *in situ* UV–Vis measurements we obtain evidence of the formation of a core–shell-type structure for the bimetallic Au–

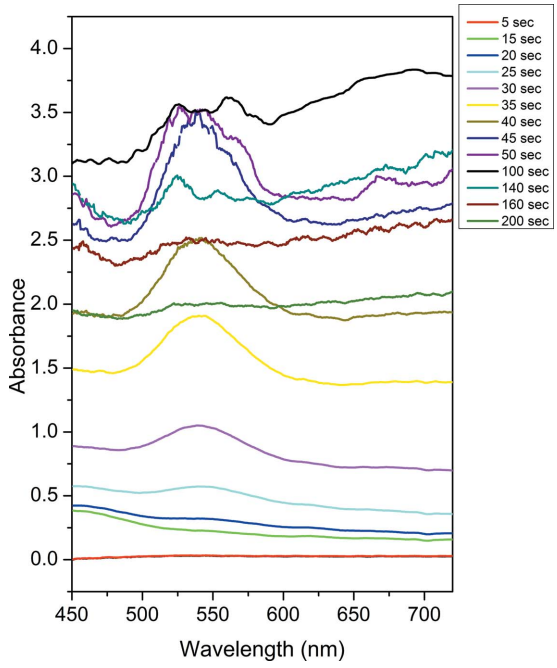

Figure 3
In situ UV–Vis spectra recorded at different time intervals during growth of the Au–Pt NPs.

Pt system. It should be noted here that Pt NPs do not show any characteristic SPR peak. Further explanation of the appearance of the two peaks or hump in the SPR spectra is given later in this paper.

The low-resolution TEM image of fully formed Au–Pt bimetallic particles extracted from the solution after 60 min of reaction is shown in Fig. S1 of the supporting information while Fig. S2 of the supporting information shows the particle size distribution histogram which reveals that most of the particles are ∼3–5 nm in size though few particles of larger sizes are also seen. Fig. 4(*a*) shows an *ex situ* HR-STEM image of a Au–Pt nanoparticle which reveals a lattice spacing of ∼0.23 nm corresponding to {111} planes. The *d*-spacings of the Au and Pt {111} plane are 2.35 Å and 2.26 Å, respectively, which are very close and it is not possible to distinguish between them by viewing the lattice spacing in a HRTEM micrograph. Hence, to distinguish between the Au and Pt regions in the particle, an EDS line scan was performed, which is explained later in this section. It should be noted that the HR-STEM/EDS measurements have been carried out on a relatively larger size particle selected from the TEM micrograph to have more clarity in the EDS spectra.

It should be noted that the particle sizes obtained in the case of these bimetallic NPs are significantly less than those of the monometallic Au and Pt NPs reported by us earlier (Nayak *et al.*, 2016). Such small sizes for Au–Pt core–shell NPs have also been reported by many researchers (Zhang & Toshima, 2013; Chen *et al.*, 2006; Gutierrez *et al.*, 2005). Zhang & Toshima (2013), for example, have reported that the smaller particle size of the Au–Pt bimetallic NPs results in higher catalytic activity for aerobic glucose oxidation. The activity increases gradually with a decrease in Au–Pt particle size from 10 nm to 3 nm and increases drastically for particle sizes of less than 3 nm since in this regime the proportion of the surface atoms, which play the main role in catalysis, increases significantly.

An EDS line scan on a representative nanoparticle is shown in Fig. 4(*b*). In EDS line scans the electron beam moves along a line on the sample surface and measures the counts of the characteristic fluorescent X-rays coming out of the elements present in the sample as a function of the beam position. The count rate is measured in the selected windows of the spectrum corresponding to the characteristic X-ray energies of the particular element expected in the sample. The variation of the X-ray count rate in the selected window corresponding to

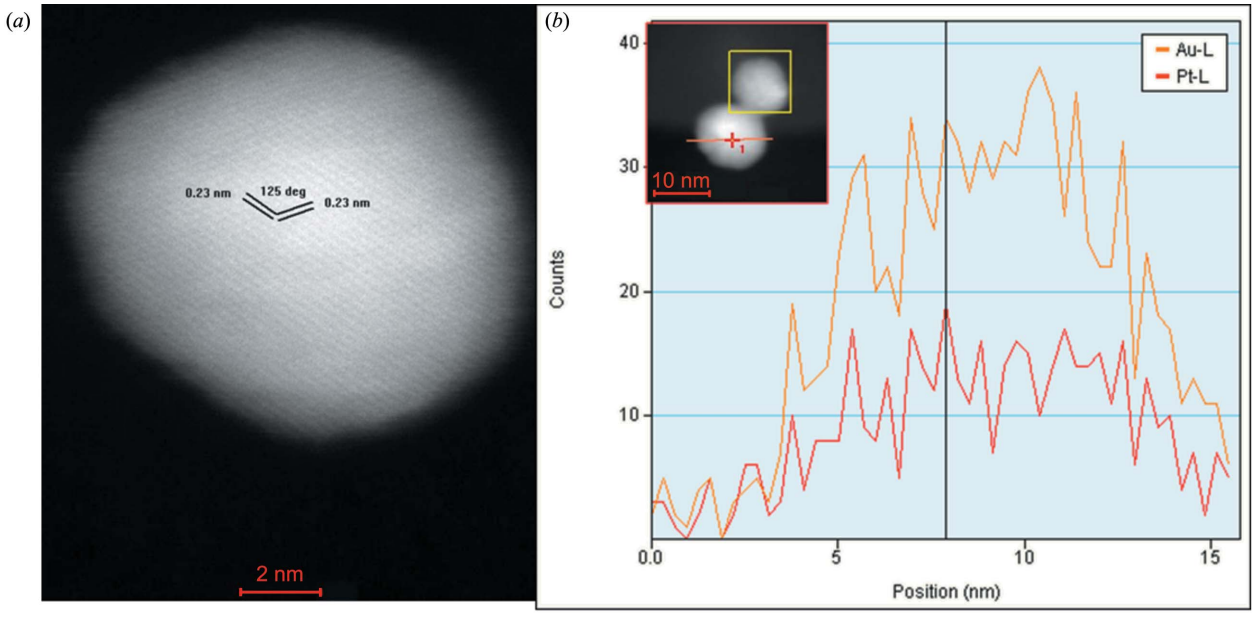

Figure 4
(*a*) HR-STEM micrograph and (*b*) EDS line scan on fully formed Au–Pt bimetallic nanocrystal.

a particular element gives the changes in concentration of that element over the line of scanning. Fig. 4(*b*) indicates a higher concentration of Au at the central portion than Pt manifesting a nearly core–shell-type structure. Our EDS line-scan spectrum resembles spectra reported by several other researchers on Au–Pt core–shell structure (Jang *et al.*, 2014; Bian *et al.*, 2015; Zhang & Toshima, 2013; Li *et al.*, 2015); however, it should be mentioned here that in the EDS line scan we have not observed any region where the Pt concentration is higher than that of Au. This suggests that the core may be Au but the shell is not entirely Pt; instead it may be a bimetallic shell of both Au and Pt or a thick Au core and a thin Pt shell. It should be noted here that the core–shell image contrast could not be seen in the HRTEM micrograph due to the very similar atomic numbers of Au and Pt.

For further insight into the structure of the particles, *ex situ* XPS measurements were carried out. Au–Pt bimetallic particles were etched with Ar^+ ions for different time intervals and the XPS spectra were recorded to see whether the surface composition changed with etching. Fig. 5(*a*) represents the XPS spectra for the Au 4*f* orbital for different etching times. The as-prepared sample with no etching shows two Au 4*f* peaks ($4f_{5/2}$ and $4f_{7/2}$) with a difference in binding energy of 3.6 eV which is a characteristic of Au (Zeng *et al.*, 2006). However, in this as-prepared sample Au is more electronegative as compared with elemental Au and there is an increment in the binding energy of Au with an increase in etching time. It has been observed that, after an etching of 105 min, the binding energy of Au $4f_{7/2}$ is ∼84.0 eV which is a characteristic of Au^0.

Fig. 5(*b*) shows the representative XPS spectra for the Pt 4*f* orbitals. It has been observed that binding energy corresponding to Pt $4f_{7/2}$ in the as-prepared sample (71.33 eV) and the difference in binding energies of the Pt $4f_{7/2}$ and Pt $4f_{7/2}$ peaks is very close to that of the Pt 0 state (Zeng *et al.*, 2006) and there is again an increment in the binding energies of the Pt 4*f* peaks as etching time is increased.

In the as-prepared sample, Au is more electronegative due to the fact that in this case the XPS signal of Au mostly comes from the Au/Pt interface of the Au core and Pt shell structure, and there is a definite electronic interaction at the Au–Pt interface. With the increase in etching time, as more and more Pt shell is removed by etching, we obtain the enhanced signature of metallic Au of the core and the binding energy of Au 4*f* peaks increases. This is also corroborated with the nature of the variation of the binding energy of the Pt 4*f* peaks, where we find that Pt was initially present as Pt metal and its binding energy increases as we approach the Au/Pt interface by etching.

Figs. 5(*c*) and 5(*d*) show the variation of intensities of the Au $4f_{7/2}$ and Pt $4f_{7/2}$ peaks with increase in etching time. The intensities are obtained after background correction and are normalized with respect to the intensity value at the maximum etching time. Intensities of both Au and Pt peaks increase with etching due to removal of the surfactants; however, it has been found that with etching the relative increase in intensity of the Au $4f_{7/2}$ peak is much higher as compared with that of the Pt

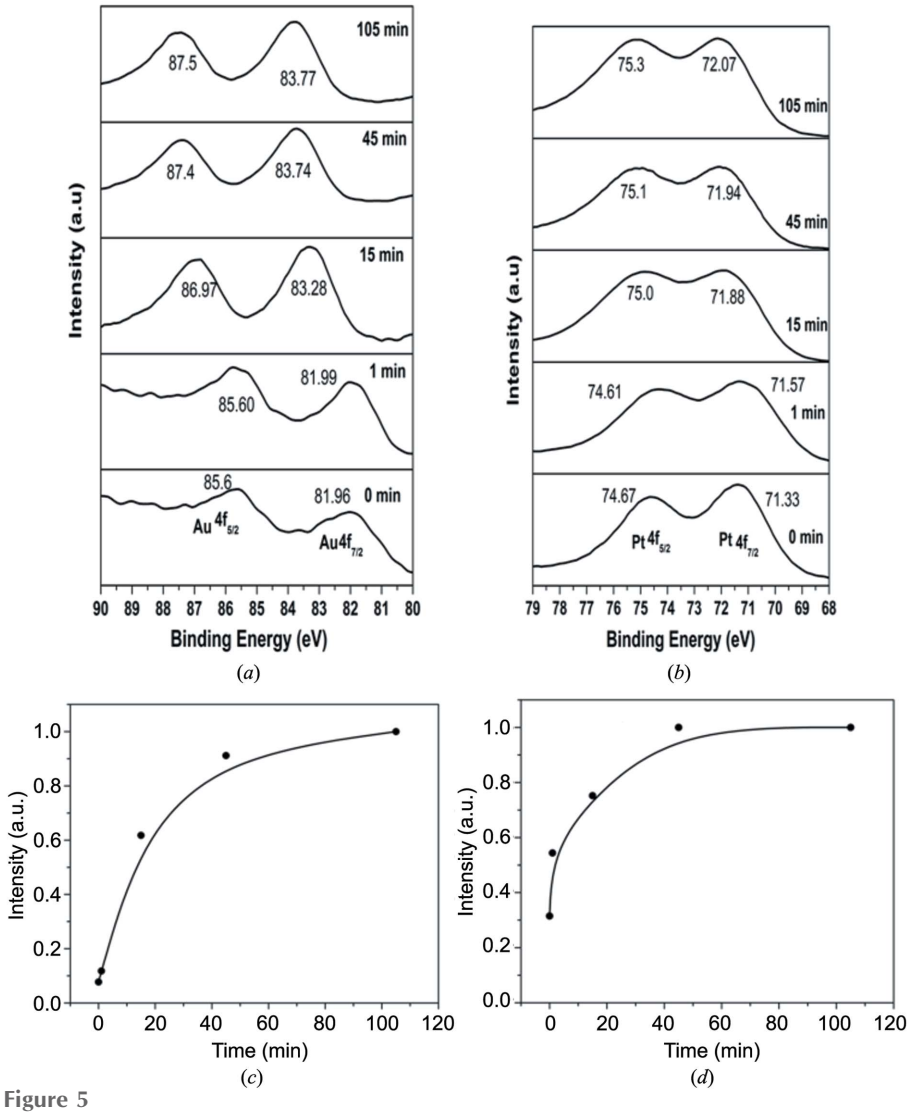

Figure 5
(*a*) Au 4*f* XPS spectra with different sputtering times: 0 min, 1 min, 15 min, 45 min and 105 min. (*b*) Pt 4*f* XPS spectra with different sputtering times: 0 min, 1 min, 15 min, 45 min and 105 min. (*c*) Variation of intensity as a function of sputtering time of the Au $4f_{7/2}$ XPS peak after background correction using a Shirley background and normalization with respect to the intensity after 105 min etching. (*d*) Variation of intensity as a function of sputtering time of the Pt $4f_{7/2}$ XPS peak after background correction using a Shirley background and normalization with respect to the intensity after 105 min etching.

$4f_{7/2}$ peak. This implies that Au is mostly present at the core and Pt at the shell of the NPs. Thus, XPS results also corroborate with the EDS line-scan results as discussed in the previous paragraph that the NPs formed have a thick Au core and thin Pt shell. The formation process of these core–shell bimetallic nanocrystals is further probed by *in situ* XAS measurements.

Fig. 6(*a*) shows the *in situ* time-resolved XANES spectra of the reaction solution measured at the Au L_3-edge. It can be seen that the near-edge spectrum of 0 s data shows a white line at 11923 eV which is due to electronic transition from the $2p_{3/2}$ to 5*d* state. This white line is a characteristic of Au^{3+} and disappears for metallic Au due to fully filled 5*d* states. The decrease in the intensity of the white line and finally its disappearance with time suggests reduction of $HAuCl_4$ and formation of metallic gold NPs. It should be noted here that, as has been mentioned above, although Au and Pt XAS spectra were taken every 1 s in the present experiment, in Fig. 6 the XANES spectra for the instants where significant changes were observed in the XANES white line features at the Au and Pt edges are only shown for clarity of the figures.

A linear combination fit of the time-resolved XANES spectra was performed using the *ATHENA* code of the *IFEFFIT* software package (Newville, 2001) in the energy range from −20 to 30 eV around the Au L_3 absorption edge, considering the XANES spectra of $HAuCl_4$ and Au foil as standards of the +3 and +0 states to obtain a quantitative measure of the presence of the two species in the reaction solution at a particular reaction time. The values of the weights of the two species were constrained between 0 and 1 and their sum was forced to 1. The goodness of fit has been determined by the parameter $R_{\rm factor}$ (Kelly *et al.*, 2008); $R_{\rm factor}$ for all the linear combination fitting at the Au L_3-edge is less than 0.01. The linear combination fittings of three representative spectra taken at 1 s, 5 s and 100 s are shown along with the residuals of the fittings in Fig. S3 of the supporting information. Fig. 7(*a*) shows the percentage of the two phases present in the reaction solution as a function of time obtained from the linear combination fitting of the time-resolved XANES spectra. From Fig. 7(*a*), it has been observed that within 6 s about 99% of the Au cations are in the metallic (+0) state and after 10 s about 100% of the Au cations are reduced to the +0 state.

Fig. 6(*b*) shows the *in situ* time-resolved XANES spectra of the reaction solution measured at the Pt L_3-edge. The near-edge spectrum of the 0 s data shows a white line at 11571 eV which is due to electronic transition from the $2p_{3/2}$ to 5*d* state. This white line is a characteristic of Pt^{4+} ions and disappears for metallic Pt due to fully filled 5*d* states. The decrease in the intensity of the white line with time suggests reduction of H_2PtCl_6 and formation of metallic Pt. A linear combination fit of the time-resolved XANES spectra was performed considering H_2PtCl_6 and Pt foil spectra as standards of the +4 and +0 states. $R_{\rm factor}$ for all the linear combination fitting at the Pt L_3-edge is less than 0.01. The linear combination fitting of three

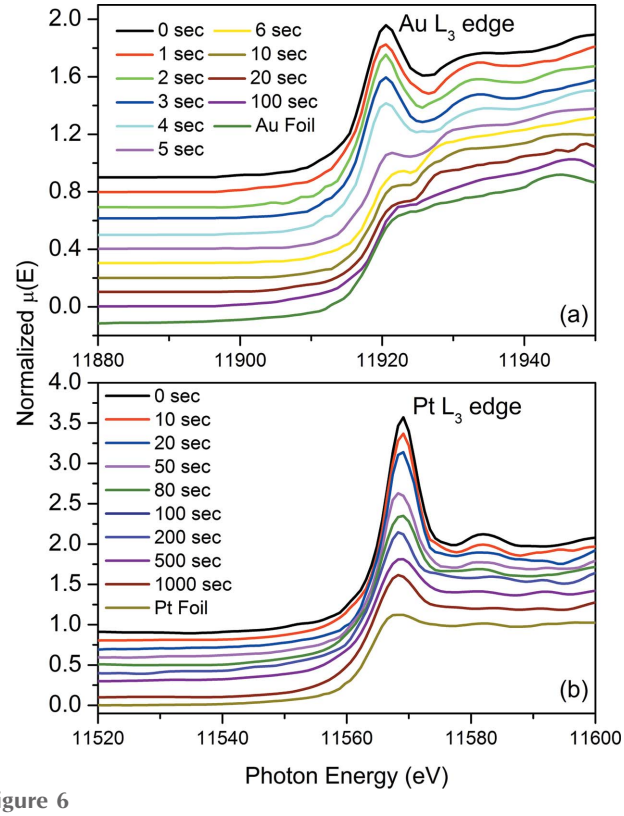

Figure 6
In situ XANES spectra at the (*a*) Au and (*b*) Pt L_3-edge recorded at different time intervals during the growth of Au–Pt NPs.

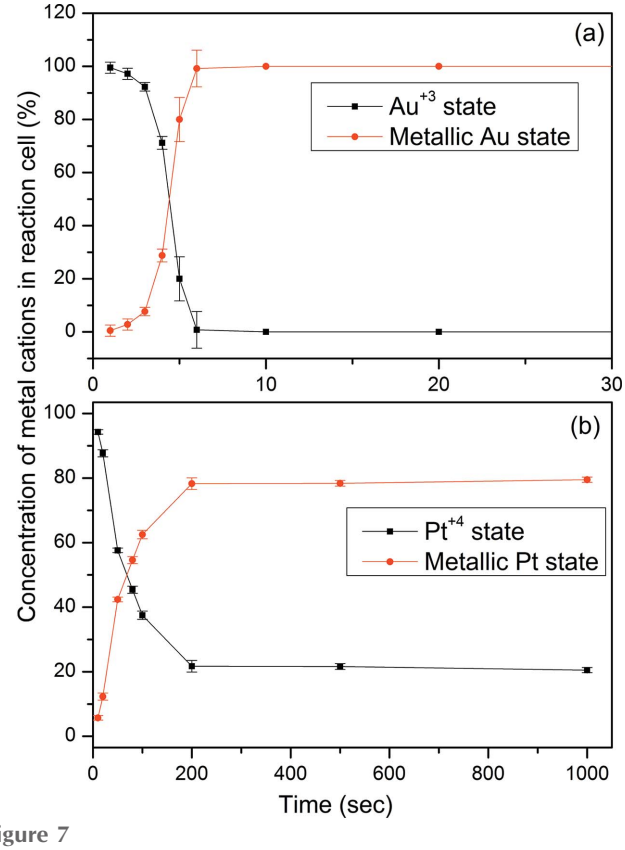

Figure 7
Linear combination fit results of *in situ* XANES spectra at the (*a*) Au and (*b*) Pt L_3-edge recorded during growth of Au–Pt NPs.

representative spectra taken at 10 s, 100 s and 1000 s have been shown along with the residual of the fitting in Fig. S4 of the supporting information. Fig. 7(*b*) shows the percentage of the two phases present in the reaction solution at different times obtained from the linear combination fitting of the time-resolved XANES spectra. It can be seen that within 10 s about 6% of the Pt cations are in the metallic (+0) state and after 200 s about 78% of the Pt cations are reduced to the +0 state.

Fig. 8 shows the experimental *in situ* EXAFS [$\mu(E)$ *versus* E] spectra recorded during the growth of Au–Pt bimetallic NPs simultaneously at the Au and Pt L_3-edges. EXAFS oscillations have been extracted from the EXAFS spectra following the standard procedure (Konigsberger & Prins, 1988). For the EXAFS oscillations, $\chi(k)$ is weighted by k^2 to amplify the oscillation at high k and the functions $\chi(k)k^2$ are Fourier transformed using the k range 2–10 Å^{-1} for the Au edge and 2–8.5 Å^{-1} for the Pt edge to generate the $\chi(r)$ *versus* r [or Fourier-transformed EXAFS (FT-EXAFS)] spectra in terms of the phase-uncorrected radial distances from the centre of the absorbing atom. The EXAFS data analysis program available within the *IFEFFIT* software package has been used for reduction and fitting of the experimental EXAFS data (Newville, 2001). The parameters used for the EXAFS data fitting are bond distance (r), coordination number (N) and Debye–Waller factor (σ^2), which give the static and thermal disorder of the system, and the goodness of fit has been determined by the parameter $R_{\rm factor}$ (Kelly *et al.*, 2008). $R_{\rm factor}$ for all fits is less than 0.01, which ensures a good fit.

Fig. 9(*a*) shows the $\chi(r)$ *versus* r plots at the Au L_3-edge at different times during the growth of gold platinum bimetallic NPs. The first peak (at ∼1.8 Å) corresponds to the Au—Cl bond and the peaks between 2 and 3 Å correspond to the Au—Au and Au—Pt bonds. The $\chi(r)$ *versus* r plots have been fitted assuming an Au–Cl path, Au–Pt path and Au–Au path. While fitting the data, bond lengths and coordination numbers of the above three shells have been varied; however, the value of the Debye–Waller factors (σ^2) has been kept fixed at 0.002 for the Au–Cl path and at 0.004 for the Au–Au and Au–Pt paths which have been found by fitting the data of the Au precursor (having only Au—Cl bonds) and Au NPs formed after 90 min of reaction (having only Au—Au and Au—Pt bonds), respectively. The value of S_0^2 has been kept fixed at 1 for all the paths of all the data at both the Au and Pt L_3-edges as obtained from the fitting of the EXAFS data of the respective precursors. The parameter ΔE_0, on the other hand, is kept the same for all the paths of data; however, it is varied during the fitting of each data set. For the Au L_3-edge, the value of ΔE_0 is found to vary in the range 4.5–7 eV over the data of different time instants, while for the Pt L_3-edge data the value of ΔE_0 is found to vary in the range 3–5 eV.

It should be noted here that the Pt L_3-edge oscillations in the high k range will have an effect on the Au L_3-edge data since the difference in the two edges is less than 500 eV. However, as has been shown by Chen *et al.* (2006), interference of Pt L_3-edge oscillations in the Au L_3-edge data results in the appearance of peaks at low $r < 2$ Å, whereas peaks due to the Au and Pt shells generally appear at $r > 2$ Å. We have also found that Au L_3-edge FT-EXAFS data of the

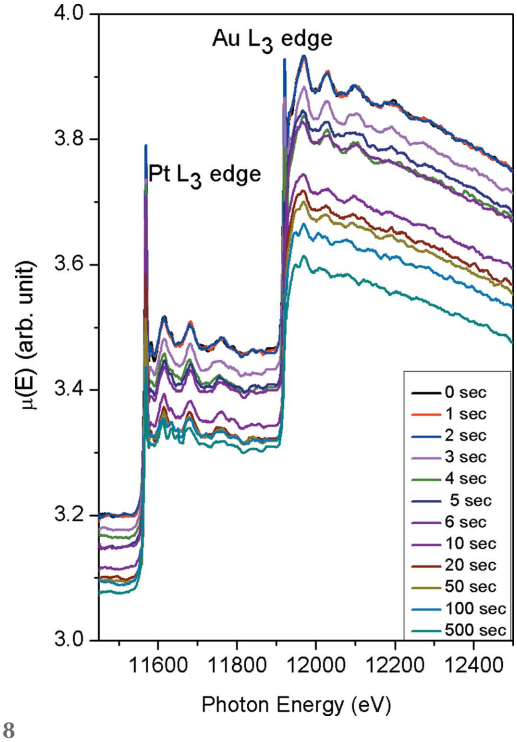

Figure 8
In situ EXAFS spectra at the Pt and Au L_3-edges recorded at different time intervals during growth of Au–Pt NPs.

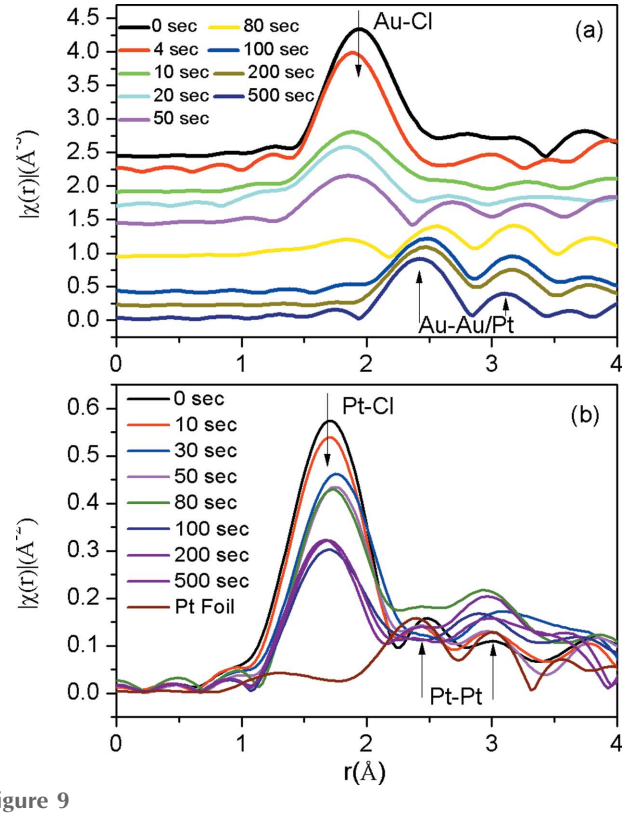

Figure 9
$\chi(r)$ *versus* r plot (FT-EXAFS spectra) measured at the (*a*) Au and (*b*) Pt L_3-edge recorded at different time intervals during growth of Au–Pt NPs.

gold precursor without any Pt precursor in the solution and the 0 s data of the reaction solution containing both Au and Pt precursors resemble each other at lower r range without any extra peak in the mixed precursor case. Therefore, we can say that Pt L_3-edge oscillations have not significantly affected the Au L_3-edge data in this case.

The theoretical fitting of two representative spectra taken at 50 s and 100 s have been shown along with contributions from different paths in Figs. S5 and S6 of the supporting information. The best-fit results have also been presented in Table S1 of the supporting information for the Au L_3-edge data. Fig. 10(*a*) shows the variation of coordination numbers of the above three shells with time. It can be seen from Table S1 that the bond lengths corresponding to the Au–Cl and Au–Pt shells do not change significantly during the reaction; however, the Au—Au bond length decreases from ~3 Å to 2.88 Å with time. A similar phenomenon has also been observed by Yao *et al.* (2010) during the growth of gold nanocrystals from $HAuCl_4$ precursor. The above authors have shown by linear combination fit of theoretically simulated XANES spectra of $HAuCl_4$ precursor and Au_2Cl_6 dimers that this initial observation of higher values of the Au—Au bond length is possibly due to the partial reduction of $HAuCl_4$, the presence of Cl^{1-} ions surrounding the Au atoms and formation of Au–Cl dimers. However, as the reaction proceeds, the specific surface area per Au atom decreases, which in turn reduces the capping efficiency of the Cl^{1-} ions, and the Au—Au bond length thus approaches its nominal value of 2.88 Å. It should be noted here that in our case the time scale observed for complete reduction of $HAuCl_4$, *i.e.* 90–100 s, as shown in Fig. 10, also agrees with the time scale given in Table S1 for the Au—Au bond to attain its nominal value of 2.88 Å. It can also be noted that the Au—Pt bond distance obtained is ~2.65 Å which is less than the nominal Pt—Pt bond distance of 2.76 Å. However, in solution while studying the formation of Pt NPs reduced by methanol in the presence of citrate, Lin *et al.* (2006) have also reported a Pt—Pt bond length value of 2.68 Å.

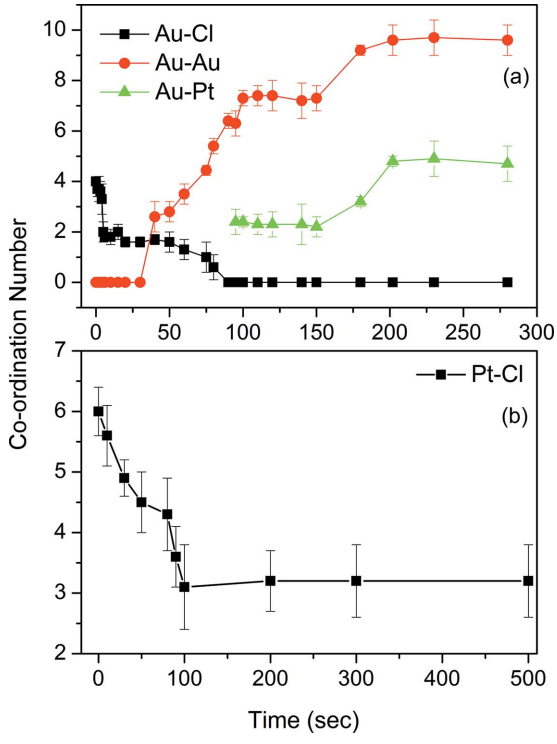

Figure 10
Variation of coordination numbers of (*a*) Au—Cl, Au—Au, Au—Pt bonds and (*b*) Pt—Cl bonds as a function of reaction time during growth of Au–Pt NPs.

Fig. 9(*b*) shows the $\chi(r)$ *versus* r plots at the Pt L_3-edge at different times during the growth of Au–Pt bimetallic NPs. The first peak (at ~1.8 Å) corresponds to the Pt—Cl bond and the peaks between 2 and 3 Å correspond to Pt—Au and Pt—Pt bonds. It should be noted that the Au L_3-edge appears only 355 eV above the Pt L_3-edge, and therefore the energy range measured above the Pt L_3-edge is limited and we can obtain a k range only up to 8.5 $Å^{-1}$ for the Pt L_3-edge EXAFS data. Since the k-range is short, we could obtain information regarding the first shell (Pt–Cl) only around the Pt sites. Thus, in this case, the $\chi(r)$ *versus* r plots have been fitted in the range 1–2.3 Å assuming a Pt–Cl path only. The values of $R_{\rm factor}$ for all fits are less than 0.01 which ensures a good fit. Fig. 10(*b*) shows the variation of the coordination number of the Pt—Cl bond. The best-fit results have also been presented in Tables S1 and S2 of the supporting information for the Au and Pt L_3-edge data, respectively.

Recently, Frenkel *et al.* (2013) have suggested a method to determine the homogeneity of bimetallic systems from EXAFS analysis by correlating Cowley's short-range-order parameter with the homogeneity of bimetallic systems. Cowley's short-range order parameter is given by

$$\alpha = 1 - \frac{N_{AB}/N_{AM}}{x_B}, \qquad (1)$$

where x_B is the molar concentration of B-type atoms in an A–B bimetallic alloy, N_{AB} is the average coordination number of B-type atoms around A-type atoms, and N_{AM} is the average coordination number of metal neighbours around A-type atoms. The Cowley parameter (α) can vary from −1 to +1 and can be used to determine the positive and negative degree of clustering in bimetallic alloys. A positive value of α indicates that the bimetallic system is heterogeneous in nature. For a homogeneous alloy, the value of α lies between $\alpha_{\rm min}$ and 0, where $-1 < \alpha_{\rm min} < 0$. In our case, we have $N_{\rm AuPt} = 4.8$, $N_{\rm AuM} = 4.8 + 9.6 = 14.4$, $x_B/x_A = 0.78$ (from XANES), and therefore $\alpha = 0.24$. The above values of the coordination numbers for different bonds have been taken after 200 s from the start of the reaction since it has been found that the coordination numbers do not change after that. The positive value of α obtained in this case indicates that Au and Pt are not homogeneously mixed; instead they form a heterogeneous configuration consistent with a core–shell structure (Frenkel *et al.*, 2013).

3.1. Growth of Au–Pt bimetallic NPs

From the XANES analysis at the Au and Pt L_3-edge (Fig. 7) it can be observed that the Au cations are reduced to a metallic state within 10 s; however, the reduction of the Pt cations during this time is only 5%. The reduction of H_2PtCl_6 is much slower and, even after a sufficiently long time of 1000 s, only 78% of Pt is reduced to a metallic state. This gives an indication that the Au seeds are formed immediately after adding the reducing agent and the Pt reduction occurs slowly on the surface of the Au seeds.

From the time-resolved EXAFS analysis at the Au L_3-edge (Fig. 10*a*) it can be seen that the Au–Cl coordination number shows a sudden drop from 4 to 2 at 5 s. This may correspond to the reduction of Au^{3+} to Au^{1+} in the early stages of the reaction which has been mentioned by many researchers during the growth of Au NPs (Ohyama *et al.*, 2011; Harada & Kamigaito, 2012). After 80 s there is no peak corresponding to the Au—Cl bond. At 40 s we see the appearance of the Au–Au peak with a sudden jump in the Au–Au coordination. The Au–Au coordination monotonically increases up to 7 until 100 s. At 100 s there is the appearance of Au–Pt coordination shell. The Au–Au and Au–Pt coordinations remain the same until 150 s, after which there is a sudden jump in the Au–Au coordination from 7 to 9 and the Au–Pt coordination increases monotonically to 4.7.

As suggested by Sakai & Alexandridis (2005), the growth mechanism of block copolymer stabilized NPs is governed by three main stages: (i) reduction of metal ions by block copolymer or additional reducing agent, (ii) absorption of block copolymer on cluster and reduction of metal ions on the surface, and (iii) growth of NPs stabilized by block copolymer. These three stages can also be identified for Au–Pt bimetallic NPs. Until 40 s from the start of the reaction, the reduction of gold precursor occurs which corresponds to the first stage described above. After 40 s there is a sudden jump of the Au–Au coordination to 2.6 which may indicate the formation of an Au_4 cluster (Ohyama *et al.*, 2011). This situation is similar to the LaMer nucleation burst (Tromp *et al.*, 2003) where the monomer concentration increases in the solution and as it crosses the critical value the nuclei are suddenly formed with a jump in the nearest-neighbour coordination. Subsequently, the Au–Au coordination number increases signifying the growth of these Au_4 clusters accompanied by the reduction of Au–Cl coordination until 100 s. This corresponds to the second stage of the process. After 100 s the appearance of Au–Pt coordination signifies the formation of the shell. However, the coordination numbers of Au–Au and Au–Pt remain constant until 150 s which may indicate the formation of a layer containing both Au and Pt between the Au core and Pt shell. At this stage, the Au–Au coordination of 7.3 is close to the coordination number of the Au_{55} cubo-octahedral cluster which is a stable cluster due to closing of the second geometrical shell (Genest *et al.*, 2009). After 150 s, there is again a sudden jump in Au–Au coordination to 9.6 which is close to the icosahedral Au_{147} cluster which is a stable cluster with a third geometrical shell closing (Petkov *et al.*, 2008). The Au–Pt coordination number also monotonically increases until 200 s signifying the growth of the Pt shell. This corresponds to the third stage of the reaction as per the above model. From the Pt L_3-edge EXAFS data (Fig. 10*b*) it can also be seen that after 100 s there is no further reduction of Pt precursor and subsequently there is a slight increase in the Pt–Cl coordination which may correspond to the stabilization of the NPs.

It should be noted here that, as per the above proposition, Au precursor is first reduced and Au_4 clusters are formed as has been confirmed by *in situ* XANES and EXAFS studies, and further growth of Au and Pt takes place on these clusters which act as seeds. However, as has been observed by Ataee-Esfahani *et al.* (2010*b*), the deposition rate of Au is much higher than that of Pt. Therefore, block copolymer preferentially attaches to $AuCl_4^-$ and reduces it on the surface of the clusters resulting in growth of the Au clusters. As the concentration of $AuCl_4^-$ ions decreases in the solution, $PtCl_6^-$ ions are available for attachment to the polymer and this results in the formation of the Pt shell. Thus, Au_{55} clusters are formed prior to Pt shell formation. However, there is also an intermediate stage when both Au and Pt are simultaneously reduced by the block copolymer. This results in a layer of Au–Pt alloy between the Au core and Pt shell. This signature of an Au–Pt alloy interface has been found by *ex situ* XPS measurements, also described earlier.

It should also be noted that, although the size of the NPs as shown by HR-STEM is $\lesssim 10$ nm, the SPR peak in the *in situ* UV–Vis spectra shown in Fig. 3 initially appears at 540 nm which corresponds to much larger particles. However, as the reaction proceeds, the SPR peak shows a blue shift and at 50 s it appears at 520 nm corresponding to <10 nm particle size. A similar phenomenon of the appearance of the SPR peak at higher wavelength and its blue shift during the reaction has been found by other workers also (Meng *et al.*, 2016). This can be attributed to the effect of the block copolymers engulfing the gold particles resulting in formation of branched intermediates during the reaction. It should be noted that from *in situ* EXAFS measurements also discussed above we have seen that Au–Au peaks start increasing from 50 s onwards. The gold particles formed before 50 s correspond to the initial stage of growth corresponding to the 'reduction of metal ions by block copolymer' stage as mentioned above and at this stage gold particles or clusters must be covered with the block copolymer. As the reaction proceeds we start obtaining spherical-like NPs with fewer branches and from 50 s onwards the SPR peak starts to appear at 520 nm corresponding to particles of 10 nm size. However, it can be seen from Fig. 3 that from 50 s onwards another peak also starts to appear at 560 nm along with the peak at 520 nm. It has been observed from *in situ* EXAFS studies that in this time interval a layer containing both Au and Pt between Au core and Pt shell also appears. *Ex situ* XPS studies also suggest that there is a Au–Pt mixed phase at the interface of the core and shell which has a different electronic configuration than that of Au and the peak at 560 nm may correspond to this phase. Subsequently, the SPR peaks vanish from 150 s onwards as the Pt shell starts covering the Au NPs. *In situ* EXAFS measurements also show

that the Au–Pt coordination starts to increase from 150 s onwards.

3.2. Comparison of growth of Au–Pt bimetallic NPs with growth of Au and Pt monometallic NPs

In our earlier communication (Nayak *et al.*, 2016), we have synthesized Au and Pt NPs following a similar synthesis route and characterized by *in situ* XAS and UV–Vis spectroscopy. Here, we attempt to compare the formation of monometallic and bimetallic NPs. In all of the cases we have identified the three stages of growth as suggested by Sakai & Alexandridis (2005). However, for monometallic NPs the process is much slower than that of the bimetallic NPs. This may be due to the use of ascorbic acid as reducing agent in the latter case, which is comparatively stronger than sodium citrate used for the synthesis of gold NPs (Nayak *et al.*, 2016). The use of a stronger reducing agent results in faster reduction of the precursor and formation of smaller nuclei. In the case of the growth of Pt monometallic NPs (Nayak *et al.*, 2016), the Pt precursor could not be reduced at room temperature with ascorbic acid as reducing agent and the reaction solution had to be heated to start the reduction of the precursor. However, in the bimetallic case, Pt precursor is reduced at room temperature only. Although the reduction is much slower than that of gold precursor, the reduction is facilitated by the formation of small Au clusters which act as seeds for the surface reduction of the Pt precursor. For the case of Au and Pt monometallic NPs, 13-atom clusters are formed which act as nuclei for further growth; however, for Au–Pt bimetallic NPs, 4-atom clusters act as nuclei for growth. This results in smaller bimetallic NPs compared with the monometallic case. The Au_{147} cluster has been identified in the growth of Au monometallic NPs, which further grow into Au NPs. In the case of Au–Pt bimetallic NPs, Au_{147} clusters are also formed which become coated with Pt shells.

4. Conclusions

Au–Pt bimetallic NPs have been synthesized through a one-pot synthesis route from their respective chloride precursors using block copolymer as a stabilizer. Using the setup for simultaneous *in situ* time-resolved XAS and UV–Vis measurements at the energy-dispersive EXAFS beamline (BL-08) at Indus-2 SRS at RRCAT, Indore, India, the growth of Au–Pt bimetallic NPs from their respective chloride precursors using block copolymer stabilizer has been studied. The measurements have been carried out in a specially designed Teflon cell with one optical path for X-rays in the direction of the synchrotron beam and another in the perpendicular direction for visible radiation. From the *in situ* measurement of UV–Vis spectroscopy, it has been observed that Au seeds are formed with the appearance of an Au SPR peak which vanishes when the Pt shell starts forming on the Au core. This confirms the formation of core–shell-like structure in Au–Pt bimetallic alloy. *Ex situ* studies by HRTEM with EDS line-scan and XPS measurements with *in situ* etching on the fully formed NPs also ascertain their core–shell-type nature. However, simultaneous *in situ* XAS measurement gives a detailed microscopic account of the phenomenon, which shows that Au precursor is reduced within 10 s and Au_4 clusters are formed which act like nuclei for further growth and the Pt reduction occurs slowly on the surface of the Au nuclei. The study of the formation process shows how the difference in the reduction potential of the two precursors could be used successfully to obtain the core–shell configuration of bimetallic alloy in a controlled fashion using a one-pot synthesis method.

Acknowledgements

The authors wish to acknowledge the DCMPMS Electron Microscopy Facility, Tata Institute of Fundamental Research, India, for the HR-STEM measurement. The authors also wish to acknowledge Dr P. Mondal of RRCAT, Indore, for his help in characterization of the samples.

References

Ataee-Esfahani, H., Wang, L., Nemoto, Y. & Yamauchi, Y. (2010*a*). *Chem. Mater.* **22**, 6310–6318.
Ataee-Esfahani, H., Wang, L. & Yamauchi, Y. (2010*b*). *Chem. Commun.* **46**, 3684–3686.
Banerjee, I., Kumaran, V. & Santhanam, V. (2015). *J. Phys. Chem. C*, **119**, 5982–5987.
Bhattacharyya, D., Poswal, A. K., Jha, S. N., Sangeeta & Sabharwal, S. C. (2009). *Nucl. Instrum. Methods Phys. Res. A*, **609**, 286–293.
Bian, T., Zhang, H., Jiang, Y., Jin, C., Wu, J., Yang, H. & Yang, D. (2015). *Nano Lett.* **15**, 7808–7815.
Boita, J., Nicolao, L., Alves, M. C. M. & Morais, J. (2014). *Phys. Chem. Chem. Phys.* **16**, 17640–17647.
Chen, C. H., Sarma, L. S., Chen, J. M., Shih, S. C., Wang, G. R., Liu, D. G., Tang, M. T., Lee, J. F. & Hwang, B. J. (2007). *ACS Nano*, **1**, 114–125.
Chen, H. M., Peng, H. C., Liu, R. S., Hu, S. F. & Jang, L. Y. (2006). *Chem. Phys. Lett.* **420**, 484–488.
Das, N. C., Jha, S. N., Bhattacharyya, D., Poswal, A. K., Sinha, A. K. & Mishra, V. K. (2004). *Sadhana*, **29**, 545–558.
Frenkel, A. I. (2012). *Chem. Soc. Rev.* **41**, 8163–8178.
Frenkel, A. I., Wang, Q., Sanchez, S. I., Small, M. W. & Nuzzo, R. G. (2013). *J. Chem. Phys.* **138**, 064202.
Genest, A., Krüger, S. & Rösch, N. (2009). *Z. Naturforsch. Teil B*, **64**, 1246–1258.
González, E., Arbiol, J. & Puntes, V. F. (2011). *Science*, **334**, 1377–1380.
Gutierrez, D. I. G., Wing, C. E., Gutierrez, G., Lisandro, L., Jose, M. R., Requejo, F. G. & Yacaman, M. J. (2005). *J. Phys. Chem. B*, **109**, 3813–3821.
Harada, M. & Kamigaito, Y. (2012). *Langmuir*, **28**, 2415–2428.
Jang, H. J., Hong, S., Ham, S., Shuford, K. L. & Park, S. (2014). *Nanoscale* **6**, 7339–7345.
Kelly, S. D., Hesterberg, D. & Ravel, B. (2008). *Methods of Soil Analysis*, Part 5, *Mineralogical Methods*, edited by A. L. Ulery and R. Drees, pp. 387–464. Madison: Soil Science Society of America.
Khalid, M., Wasio, N., Chase, T. & Bandyopadhyay, K. (2010). *Nanoscale Res. Lett.* **5**, 61–67.
Konigsberger, D. C. & Prins, R. (1988). *X-ray Absorption: Principles, Applications, Techniques of EXAFS, SEXAFS and XANES*. New York: Wiley.
Lang, H. F., Maldonado, S., Stevenson, K. J. & Chandler, B. D. (2004). *J. Am. Chem. Soc.* **126**, 12949–12956.

Li, Y., Ding, W., Li, M., Xia, H., Wang, D. & Tao, X. (2015). *J. Mater. Chem. A*, **3**, 368–376.
Lim, B., Jiang, M., Camargo, P. H. C., Cho, E. C., Tao, J., Lu, X., Zhu, Y. & Xia, Y. (2009). *Science*, **324**, 1302–1305.
Lin, C. S., Khan, M. R. & Lin, S. D. (2006). *J. Colloid Interface Sci.* **299**, 678–685.
Liu, X., Wang, D. & Li, Y. (2012). *Nano Today* **7**, 448–466.
Ma, J., Zou, Y., Jiang, Z., Huang, W., Li, J., Wu, G., Huang, Y. & Xu, H. (2013). *Phys. Chem. Chem. Phys.* **15**, 11904–11908.
Meng, X., Baride, A. & Jiang, C. (2016). *Langmuir*, **32**, 6674–6681.
Nayak, C., Bhattacharyya, D., Jha, S. N. & Sahoo, N. K. (2016). *J. Synchrotron Rad.* **23**, 293–303.
Newville, M. (2001). *J. Synchrotron Rad.* **8**, 322–324.
Ohyama, J., Teramura, K., Higuchi, Y., Shishido, T., Hitomi, Y., Kato, K., Tanida, H., Uruga, T. & Tanaka, T. (2011). *ChemPhysChem*, **12**, 127–131.
Omori, T., Ando, K., Okano, M., Xu, X., Tanaka, Y., Ohnuma, I., Kainuma, R. & Ishida, K. (2011). *Science*, **333**, 68–71.
Petkov, V., Bedford, N., Knecht, M. R., Weir, M. G., Crooks, R. M., Tang, W., Henkelman, G. & Frenkel, A. (2008). *J. Phys. Chem. C*, **112**, 8907–8911.
Polte, J., Ahner, T. T., Delissen, F., Sokolov, S., Emmerling, F., Thünemann, A. F. & Kraehnert, R. (2010). *J. Am. Chem. Soc.* **132**, 1296–1301.
Qian, L., Sha, Y. & Yang, X. (2006). *Thin Solid Films*, **515**, 1349–1353.
Sakai, T. & Alexandridis, P. (2005). *J. Phys. Chem. B*, **109**, 7766–7777.
Sankar, M., Dimitratos, N., Miedziak, P. J., Wells, P. P., Kiely, C. J. & Hutchings, G. J. (2012). *Chem. Soc. Rev.* **41**, 8099–8139.
Stamenkovic, V. R., Fowler, B., Mun, B. S., Wang, G., Ross, P. N., Lucas, C. A. & Marković, N. M. (2007). *Science*, **315**, 493–497.
Tao, F., Grass, M. E., Zhang, Y., Butcher, D. R., Renzas, J. R., Liu, Z., Chung, J. Y., Mun, B. S., Salmeron, M. & Somorjai, G. A. (2008). *Science*, **322**, 932–934.
Toshima, N., Kushihashi, K., Yonezawa, T. & Hirai, H. (1989). *Chem. Lett.* **18**, 1769–1772.
Toshima, N. & Yonezawa, T. (1998). *New J. Chem.* **22**, 1179–1201.
Tromp, M., Sietsma, J. R. A., van Bokhoven, J. A., van Strijdonck, G. P. F., van Haaren, R. J., van der Eerden, A. M. J., van Leeuwen, P. W. N. M. & Koningsberger, D. C. (2003). *Chem. Commun.* pp. 128–129.
Yao, T., Sun, Z., Li, Y., Pan, Z., Wei, H., Xie, Y., Nomura, M., Niwa, Y., Yan, W., Wu, Z., Jiang, Y., Liu, Q. & Wei, S. (2010). *J. Am. Chem. Soc.* **132**, 7696–7701.
Zeng, J., Yang, J., Lee, J. Y. & Zhou, W. (2006). *J. Phys. Chem. B*, **110**, 24606–24611.
Zhang, H. J., Okumura, M. & Toshima, N. (2011*a*). *J. Phys. Chem. C*, **115**, 14883–14891.
Zhang, H. J., Okuni, J. & Toshima, N. (2011*b*). *J. Colloid Interface Sci.* **354**, 131–138.
Zhang, H. & Toshima, N. (2013). *J. Colloid Interface Sci.* **394**, 166–176.
Zhang, H. J., Watanabe, T., Okumura, M., Haruta, M. & Toshima, N. (2012). *Nat. Mater.* **11**, 49–52.